nature communications

Article

https://doi.org/10.1038/s41467-025-65856-z

Breaking the symmetry of high-entropy alloy surfaces for compressively strain-tuned oxygen reduction reaction

Received: 9 August 2024

Accepted: 23 October 2025

Published online: 02 December 2025

Check for updates

Lin He[1,5], Menggang Li[1,2,5], Longyu Qiu[1,5], Xue Ren[1], Fenyang Tian[1], Jie Sheng[3], Yequn Liu[4], Mingchuan Luo[2], Xin Zhou[1], Yongsheng Yu[1] ✉, Weiwei Yang[1] ✉ & Shaojun Guo[2] ✉

A largely unexplored approach for optimizing surface strains on terrace-type catalysts is the break of atomic symmetry to release surface stress. The key challenge lies in how to implement this approach into practical nanocatalysts, in particular the promising high-entropy alloys (HEAs). Herein, we design and synthesize a series of HEA nanorings (NRs) with abundant terrace-type defects for oxygen reduction reaction (ORR) electrocatalysis. The asymmetry-triggered release of surface stress enables the modulation of compressive strain for optimizing the electronic structure. On the optimally-tuned PtPdFeCoNi HEA NRs, we achieve mass and specific activities of 0.99 A $mg^{-1}_{platinum\ group\ metal\ (PGM)}$ and 1.32 mA cm^{-2}_{PGM} at 0.95 V versus reversible hydrogen electrode (vs. RHE), demonstrating a competitive performance. Experimental and theoretical investigations unveil that the stress-released compressive strain lowers the *d*-band center of Pt sites in HEA NRs, resulting in favorable desorption of oxygenated intermediates and thus accelerated ORR kinetics.

Anion exchange membrane fuel cells (AEMFCs) have been considered as a highly up-and-coming technology for relieving the increasingly energy and environmental crises due to their high energy efficiency and pollution-free features[1–4]. However, the widespread deployment of such sustainable energy devices is hampered by the cathodic oxygen reduction reaction (ORR) kinetic barriers and high cost of Pt electrocatalysts[5–7]. Specifically, the high ORR overpotential originates from the strong adsorption of oxygenated intermediates, which occupy substantial active sites and block proton and electron transfer, thus requiring high dosages of Pt to accelerate ORR[8]. Given that the adsorption strength of the oxygenated species depends on the position of the *d*-band center of Pt, modulating the distribution of *d*-electrons in Pt to optimize the adsorption strength by strain and/or ligand effects is desirable[9]. Constructing Pt–M alloys (M = transition metals) can effectively ameliorate the electronic structure of the Pt sites aided by the ligand effect, *yet* the restricted compositional scope of M hampers the capability of electron modulation, and thus fail to achieve summit catalytic behaviors[10,11].

High-entropy alloys (HEAs) are promising materials for further enhancing ORR activity and stability relative to traditional alloys due to their flexibility in controlling composition and concentration, stronger ligand effect, and more stable structures in terms of thermodynamics[12–15]. It has been well established that manipulating surface strain can further modify the electronic structures and reactivity of surface atoms[16–18]. However, the weak intrinsic strain effects on the perfect (111) surfaces of conventional random HEAs make it

[1]State Key Laboratory of Urban Water Resource and Environment, School of Chemistry and Chemical Engineering, Harbin Institute of Technology, Harbin, Heilongjiang, China. [2]School of Materials Science and Engineering, Peking University, Beijing, China. [3]Laboratory for Space Environment and Physical Science, Research Center of Basic Space Science, Harbin Institute of Technology, Harbin, China. [4]Analytical Instrumentation Center, State Key Laboratory of Coal Conversion, Institute of Coal Chemistry, Chinese Academy of Sciences, Taiyuan, Shanxi, China. [5]These authors contributed equally: Lin He, Menggang Li, Longyu Qiu. ✉e-mail: ysyu@hit.edu.cn; yangww@hit.edu.cn; guosj@pku.edu.cn

challenging to further maximize the ORR performance. Remarkably, the presence of imperfections, such as terrace-type defects, can break the surface atomic symmetry and induce the release of intrinsic surface stress, enabling the modulation of surface strains and accordingly the electronic structure[19,20]. Therefore, breaking the surface symmetry of HEAs via the rational deployment of abundant terrace-type edges/surfaces to optimize surface strains is desirable for highly active and durable ORR electrocatalysts, yet remains a formidable challenge.

Herein, a class of HEA nanorings (NRs) catalysts with abundant atomic terrace-type defects on both interior and outside edges were designed to enhance ORR electrocatalysis. We find that the asymmetric terrace-type defects determined as (221) facets mediated the release of surface stress and the generation of compressive strain, endowing the HEA NRs with outstanding ORR catalytic performance. Specifically, representative PtPdFeCoNi HEA NRs deliver a high mass activity of 0.99 A mg^{-1}_{PGM} at 0.95 V versus reversible hydrogen electrode (vs. RHE), 5.3 times higher than that of (111) facet-exposed nanoparticle (NP) counterparts. Theoretical calculations further unveil that the intrinsic compressive strain on the terrace surface of PtPdFeCoNi HEA NRs leads to the downshifted *d*-band center of Pt sites, weakening the OH adsorption on terrace sites, thus minimizing the ORR barrier.

Results

Material synthesis and characterizations

Selective epitaxial growth in combination with inhomogeneous oxidative etching enabled the deployment of abundant terrace-type defects on the surfaces of Pt-based HEAs (Details in Experimental Section). To decipher the growth mechanism of the PtPdFeCoNi HEA NRs, transmission electron microscopy (TEM) and inductively coupled plasma optical emission spectroscopy (ICP-OES) were conducted to characterize the products collected from different reaction stages (Supplementary Figs. 1,2). It can be concluded that the growth for HEA NRs can be divided into four major steps (Fig. 1a), involving the initial formation of Pd-rich nanosheets, the formation of concave nanosheets driven by preferential deposition of Pt atoms at the periphery of the nanosheets, the oxidative etching of nanosheets by the coaction of Br^- and O_2, and subsequent formation of uniform HEA NRs driven by the atomic diffusion process[21].

TEM and high-angle annular dark-field scanning TEM (HAADF-STEM) images show that as-prepared products are shaped in uniformly dispersed hexagonal nanoring with a thickness of ~2.13 nm (Fig. 1b and Supplementary Fig. 3a–d). On the interior and outside of the PtPdFeCoNi HEA NRs, the jagged edges are equipped with abundant terrace-type defects and terrace atoms (Fig. 1c). The interior body lattice spacing (d), measured as 0.225 nm, can be assigned to (111) facet of fcc Pt, in agreement with the X-ray diffraction (XRD) pattern (Supplementary Fig. 3e). To probe the precise structure of the PtPdFeCoNi HEA NRs, the atomic-level analysis was supported by an aberration-corrected (AC) HAADF-STEM. The imperfect (111) surfaces with (110) type step facets can be expressed as n(111)–(110), where n is the number of atomic rows on the (111) terrace[19]. In this work, the n is principally identified as 3, indicating the stepped surfaces on the interior and outside of the PtPdFeCoNi HEA NRs can be assigned to the (221) facets (Fig. 1d and Supplementary Fig. 4). The STEM energy-dispersive X-ray spectrometry (STEM-EDS) elemental mappings of PtPdFeCoNi HEA NRs manifest the homogenous distribution of Pt, Pd, Fe, Co, and Ni elements throughout the nanoring, further substantiating the high-entropy and terrace-type-defect surface structure (Fig. 1e and Supplementary Fig. 5). The composition of PtPdFeCoNi HEA NRs was further ensured to be Pt:Pd:Fe:Co:Ni = 25.5:33.1:16.5:9.4:15.5 by ICP-OES and STEM-EDS, indicating the formation of well-defined HEAs (Supplementary Fig. 3f).

It is well documented that intrinsic tensile surface stresses generally induce pressure on the order of 10^5 atmospheres on the surface atoms for platinum group metals (PGMs), contributing to a strong

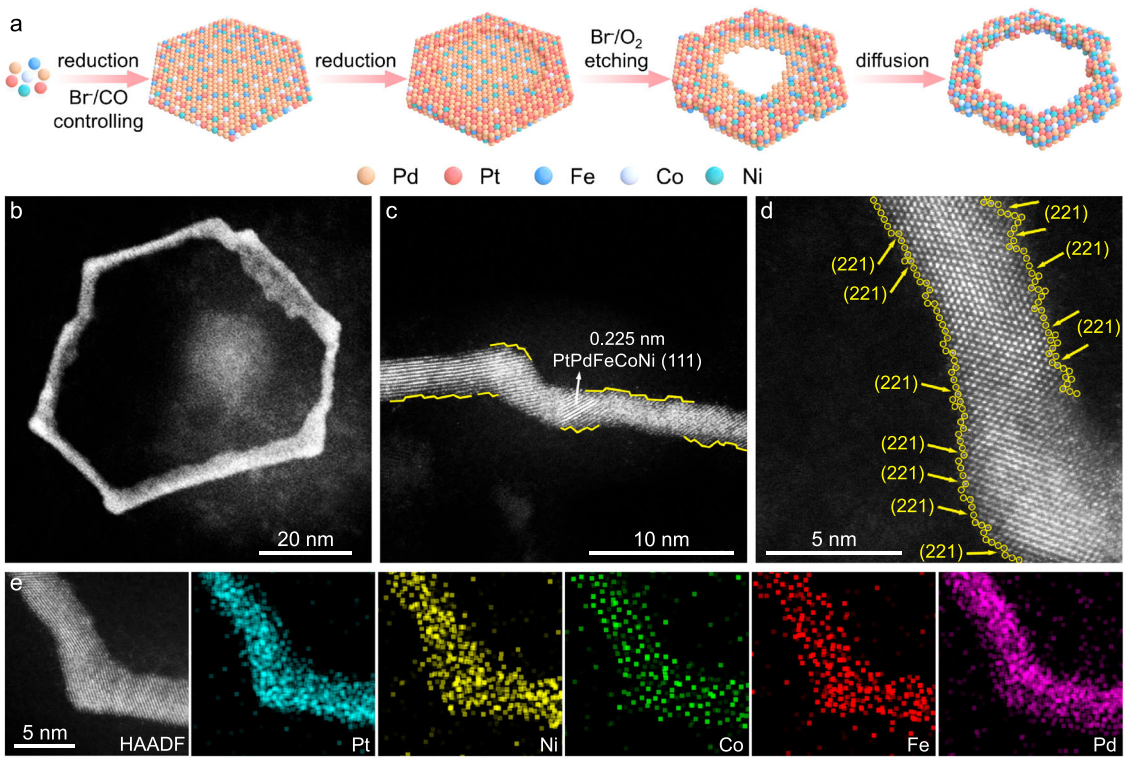

Fig. 1 | Synthesis and characterizations of PtPdFeCoNi HEA NRs. a Schematic illustration of the formation mechanism of PtPdFeCoNi HEA NRs. **b** Enlarged HAADF-STEM, **c** high-resolution HAADF-STEM and **d** AC-HAADF-STEM images of an individual PtPdFeCoNi HEA NR. **e** High-resolution EDS elemental mapping of a single PtPdFeCoNi HEA NR.

https://doi.org/10.1038/s41467-025-65856-z

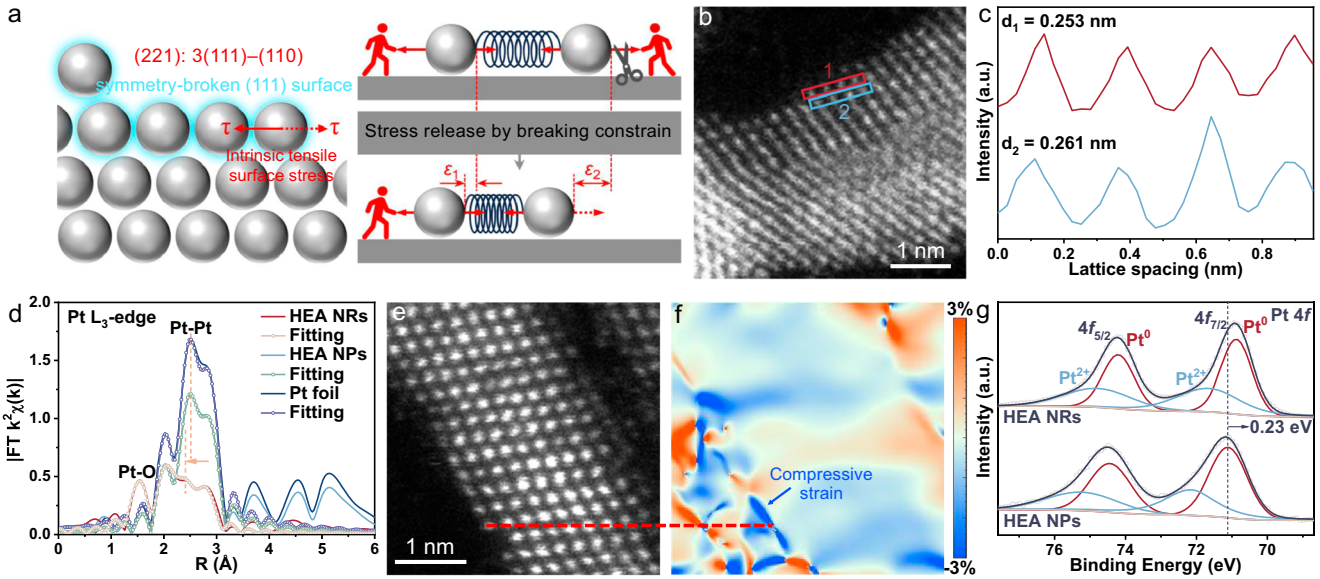

Fig. 2 | Strained and electro-structural analyses of PtPdFeCoNi HEA NRs. a The mechanism of spontaneous surface stress (τ) release by breaking symmetry constraints and simultaneous generation of compressive surface strain (ε). **b** Atomic-resolution AC-HAADF-STEM image of the surface atomic arrangement on an individual PtPdFeCoNi HEA NR. **c** Integrated pixel intensities and calculated average interatomic spacings taken from the red and azure solid rectangles in **b**, respectively. **d** FT-EXAFS spectra of PtPdFeCoNi HEA NRs and PtPdFeCoNi HEA NPs at Pt L_3-edge. **e** Atomic-resolution AC-HAADF-STEM image and **f** corresponding e_{yy} strain component of PtPdFeCoNi HEA NRs (blue represents compressive strain and orange represents tensile strain). **g** Pt 4*f* XPS spectra of PtPdFeCoNi HEA NRs and PtPdFeCoNi HEA NPs.

driving force for surface energy reduction and surface contraction[20]. This surface pressure can induce the release of stress at the asymmetric terrace-type defects of PtPdFeCoNi HEA NRs, driving the relaxation of terrace atoms and the consequent generation of compressive strain fields (Fig. 2a).

In order to demonstrate the existence of compressive strain due to terrace-like imperfections on PtPdFeCoNi HEA NRs surfaces, the integrated pixel intensities were employed to analyze the atomic arrangements at the edges. The detailed statistical analyses of average terrace-atom spacings and adjacent interior body-atom spacings reveal the presence of ~−3.2% intrinsic compressive strain on the surfaces of PtPdFeCoNi HEA NRs (Fig. 2b,c and Supplementary Fig. 6). The particular compressive strain was also verified by EXAFS characterization. The Fourier transforms of extended X-ray absorption fine structure (FT-EXAFS) spectra and corresponding fitting curves display the shortened Pt-Pt bond of the Pt-Pt scattering in the PtPdFeCoNi HEA NRs relative to those of the PtPdFeCoNi HEA NPs and Pt foil, reflecting the presence of atomic compressive strain on the surfaces of PtPdFeCoNi HEA NRs (Fig. 2d and Supplementary Fig. 7). The corresponding fitting parameters can be inspected in Supplementary Table 1. Wavelet transform (WT) of k space data macroscopically also reveals the shortened Pt-Pt bonds in the PtPdFeCoNi HEA NRs (Supplementary Fig. 8). In addition, the geometric phase analysis (GPA) manifests that the atomic compressive strain is mainly distributed at the defects of PtPdFeCoNi HEA NRs surfaces (Fig. 2e,f and Supplementary Fig. 9). The smaller average lattice parameters and positively shifted diffraction peaks of PtPdFeCoNi HEA NRs relative to those of PtPdFeCoNi HEA NPs further confirm that compressive strain can be generated in PtPdFeCoNi HEA NRs (Supplementary Fig. 10). XPS analysis was further carried out to investigate the electronic structure of PtPdFeCoNi HEA NRs. The Pt 4*f*, Pd 3*d*, and Ni 2*p* of PtPdFeCoNi HEA NRs exhibit negative chemical shifts relative to those of PtPdFeCoNi HEA NPs, whereas the Fe 2*p* and Co 2*p* display positive chemical shifts, indicating the electrons are transferred from Fe/Co to Pt/Pd/Ni atoms in PtPdFeCoNi HEA NRs (Fig. 2g and Supplementary Fig. 11). Taken cumulatively, we fashioned the PtPdFeCoNi HEA into nanoring structures equipped with plentiful terrace-type defects on the surfaces to successfully implement the symmetry-breaking approach and drive the surface compressive strain by inducing stress release.

The present synthetic strategy for HEA NRs featuring abundant terrace-type surfaces also allows for the expansion of the compositional space of HEA by introducing the corresponding precursor in the standard synthesis. The representative products are the septenary PtPdMnFeCoNiZn HEA NRs, which also have abundant terrace defects on the interior and outside surfaces (Supplementary Fig. 12). Furthermore, the $W(CO)_6$ plays an indispensable role in forming PdPt-based 2D nanoring structures, confirmed by the fact that only PtPdFeCoNi HEA nanoparticle assemblies (NPs, contrast catalysts in this work) were generated under the absence of $W(CO)_6$ in the reactant (Supplementary Fig. 13) as well as the products of mixing of nanorings and holed nanosheets caused by incomplete oxidative etching after $Mo(CO)_6$ replacing $W(CO)_6$ (Supplementary Fig. 14). The close-packed atoms assemble the surfaces of as-obtained PtPdFeCoNi HEA NPs and can be attributed to the perfect (111) facets. Moreover, the composition of PtPdFeCoNi HEA NPs was determined to be Pt:Pd:Fe:Co:Ni = 21.5:31.3:17.7:11.1:18.4, similar to that of the PtPdFeCoNi HEA NRs.

ORR electrocatalytic performance

The electrochemically active surface areas (ECSAs) of PtPdFeCoNi HEA NRs/C, PtPdFeCoNi NPs/C, and commercial Pt/C were determined to be 75.09, 45.71, and 68.72 $m^2\ g^{-1}_{Pt+Pd}$, respectively, according to the CO stripping curves (Supplementary Fig. 15). The PtPdFeCoNi HEA NRs possess the largest ECSA among these three catalysts, owing to their thin character, also revealing the high utilization of precious metals Pt and Pd[22].

The ORR polarization curves show that PtPdFeCoNi HEA NRs possess a high half-wave potential ($E_{1/2}$) of 0.959 V (vs. RHE), almost 42 and 105 mV higher than that of PtPdFeCoNi HEA NPs and commercial Pt/C (Fig. 3a & Supplementary Figs. 18,19). The smallest Tafel slope of PtPdFeCoNi HEA NRs implies that the compressive strain driven by stress release delivers the notable weakening of oxygenated intermediate adsorption and significant enhancement of reaction kinetics (Fig. 3b). The mass and specific activities were further derived to

https://doi.org/10.1038/s41467-025-65856-z

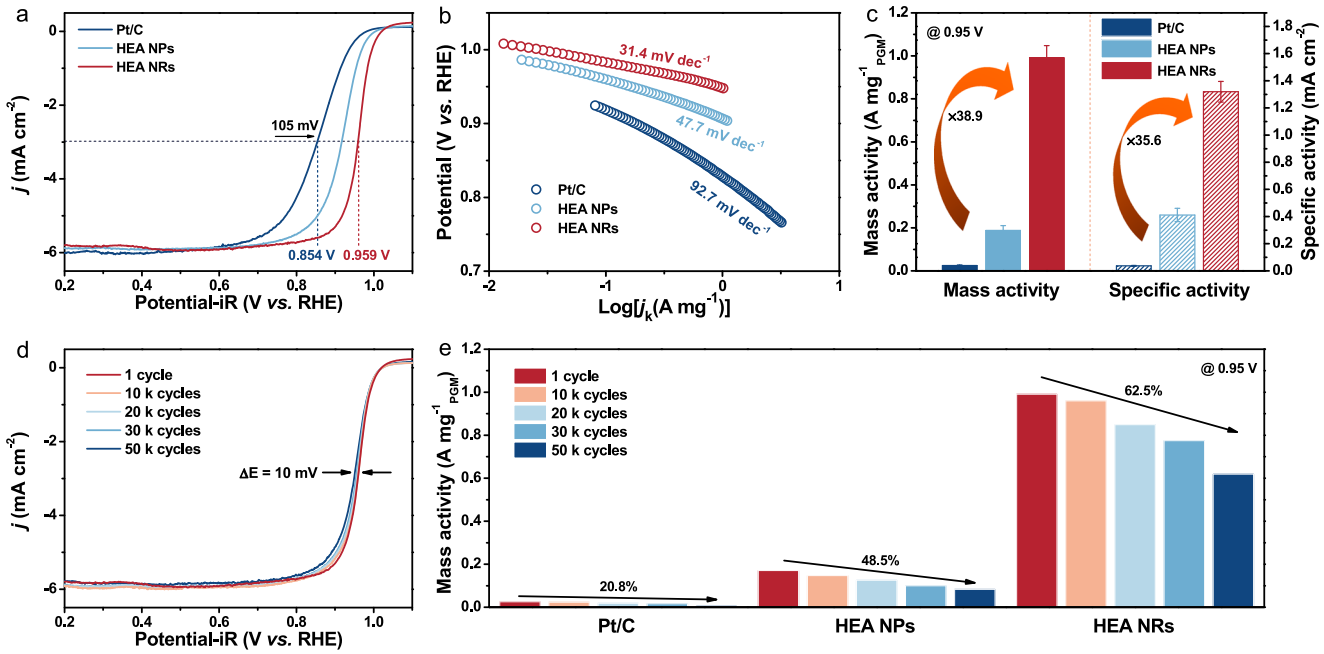

Fig. 3 | ORR performances of different catalysts in alkaline electrolytes. a ORR polarization curves in O_2-saturated 0.1 M KOH electrolyte at 25 °C, with a rotation rate of 1600 rpm and a positive scan rate of 20 mV s^{-1}, **b** Tafel plots and **c** comparison of ORR mass and specific activities at 0.95 V vs. RHE of PtPdFeCoNi HEA NRs, PtPdFeCoNi HEA NPs and commercial Pt/C catalysts. The error bars represent the standard deviation of three independent measurements. **d** ORR polarization curves of HEA NRs before and after different potential cycles. **e** The normalized mass activity changes and the activity retention of HEA NRs, NPs, and commercial Pt/C catalysts at 0.95 V (vs. RHE) before and after different potential cycles. The solution resistance was measured to be 40.7 ± 1.9 Ω.

quantify the intrinsic ORR activity (Fig. 3c and Supplementary Table 2). To assess the catalytic activity and economic benefits of Pt/Pd-based electrocatalysts fairly, we normalized the mass activities of various catalysts by the total mass of PGM elements (i.e., Pt and Pd). Since the universally chosen potential (0.9 V) is too close to the diffusion limit region to provide reliable dynamic current density due to the fast kinetic of PtPdFeCoNi HEA NRs, we evaluated the activity at 0.95 V to eliminate the O_2 diffusion limit[23]. Specifically, PtPdFeCoNi HEA NRs deliver a high mass activity of 0.99 A mg^{-1}_{PGM} at 0.95 V vs. RHE, 5.3 and 38.9 times higher than those of PtPdFeCoNi HEA NPs and commercial Pt/C, respectively. Moreover, the specific activity of PtPdFeCoNi HEA NRs is calculated to be 1.32 mA cm^{-2}, superior to PtPdFeCoNi HEA NPs (0.41 mA cm^{-2}). Of note, herein the more appropriate multi-metal-synergy ligand effect endows PtPdFeCoNi HEA NRs with high ORR performance to the PtPd, PtPdFe, PtPdCo, and PtPdFeCo low- and medium-entropy-alloy NRs (Supplementary Fig. 20 and Supplementary Table 3). In addition, PtPdFeCoNi HEA NRs exhibit elemental percentage-dependent ORR electrocatalytic activity (Supplementary Fig. 21). PtPdFeCoNi HEA NRs also show a competitive ORR performance with previously reported catalysts (Supplementary Table 4). The good performance in acidic electrolytes also reflects the encouraging potential applications of PtPdFeCoNi HEA NRs (Supplementary Fig. 24).

The cyclic voltammogram (CV) curves of PtPdFeCoNi HEA NRs and PtPdFeCoNi HEA NPs were tested to further visualize the difference of binding strength towards oxygenated intermediates (Supplementary Fig. 25). The H_{upd} peak of PtPdFeCoNi HEA NRs is negatively shifted relative to that of PtPdFeCoNi HEA NPs, suggesting the weakened adsorption of hydrogen intermediate on PtPdFeCoNi HEA NRs (left of Supplementary Fig. 25b). Meanwhile, the positive shift in the hydroxide adsorption and oxide reduction peaks of HEA NRs further witnesses the weakened PGM-O binding compared with the HEA NPs (right of Supplementary Fig. 25b). Therefore, the validated appropriate binding strength of adsorbed oxygenated intermediates logically manipulates the impressive ORR activity.

The durability analysis of PtPdFeCoNi HEA NRs was performed by electrochemical accelerated durability tests (ADTs). Notably, PtPdFeCoNi HEA NRs display only a 10 mV shift in $E_{1/2}$, even after undergoing 50 k ADT cycles, which is in contrast with the notable negative shifts observed in PtPdFeCoNi HEA NPs (Fig. 3d and Supplementary Fig. 26). Furthermore, PtPdFeCoNi HEA NRs exhibit higher conservation rate of 62.5% (50 k, MA). Notably, the delicate nanoring structure with abundant symmetry-broken terrace-type defects on interior and exterior surfaces of PtPdFeCoNi HEA NRs can be well preserved (Supplementary Figs. 27,28). This impressive structural stability can guarantee the sustained effect of particular atomic compressive strain driven by the stress release at the terrace-type defects on ORR electrocatalysis. In addition, the similar compositional distributions before and after durability tests reflect that PtPdFeCoNi HEA NRs retain the HEA phase structure without apparent elemental segregation, further confirming the impressive structural and compositional stability of PtPdFeCoNi HEA NRs (Supplementary Table 5). The high ORR stability of PtPdFeCoNi HEA NRs is attributed to their unique nanoring profile with abundant symmetry-broken terrace-type defects and thermodynamically stable high-entropy alloy structure, which can effectively resist the deformation of elaborate surface structure, deliver continuously atomic compressive strain, and simultaneously maintain a high mass/charge transport efficiency.

Insights into the oxygen reduction mechanism

To gain insight into the origin of the high ORR performance upon PtPdFeCoNi HEA NRs with particular compressive strain, density functional theory (DFT) calculations were employed. Considering that the terrace-type (221) facets with compressive strain driven by stress release dominate the surfaces of PtPdFeCoNi HEA NRs, the strained PtPdFeCoNi HEA (221) and PtPdFeCoNi HEA (111) surfaces were constructed as calculation models (Supplementary Fig. 29). Bader charge simulation reveals efficient electron transfer between elements, with Pt atoms exhibiting more negative charge states, indicating greater electron localization around them, which is

https://doi.org/10.1038/s41467-025-65856-z

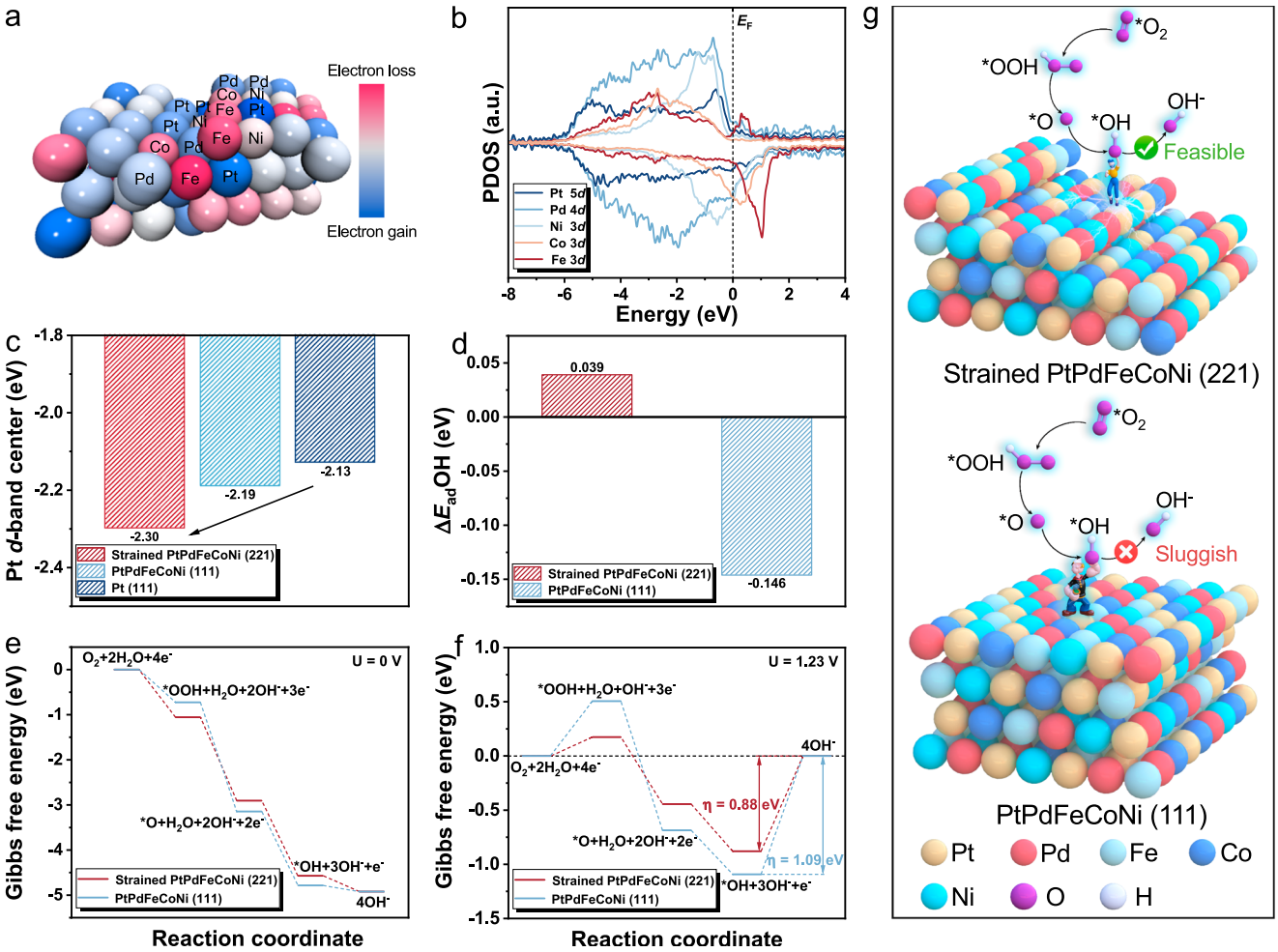

Fig. 4 | DFT calculations for the structural configuration and energetic reaction pathways. a The Bader charge simulation for strained PtPdFeCoNi HEA (221). **b** The PDOSs of strained PtPdFeCoNi HEA (221). **c** Comparison of *d*-band centers. **d** The $_{ad}$OH adsorption energy comparison on strained PtPdFeCoNi HEA (221) and PtPdFeCoNi HEA (111). The Gibbs free energetic pathways for alkaline four-electron ORR based on strained PtPdFeCoNi HEA (221) and PtPdFeCoNi HEA (111) in **e** zero electrode potential (U = 0 V) and **f** equilibrium potential (U = 1.23 V). **g** Schematic diagram of the attenuation of OH adsorption and enhancement of ORR performance on terrace Pt sites of PtPdFeCoNi HEA NRs.

consistent with XPS analysis (Fig. 4a). This is attributed to surface terrace defects of PtPdFeCoNi HEA NRs, which can break the symmetry and induce attractive interactions between surface atoms and charge redistribution, thus optimizing the electronic structures of surface Pt atoms. The projected partial density of states (PDOSs) further reveals the detailed electronic contributions of PtPdFeCoNi HEA NRs (Fig. 4b). The efficient *d*-*d* orbital coupling between each element in PtPdFeCoNi HEA NRs lowers the energy barrier for electron transfer from the HEA surfaces toward the adsorbates, leading to significant improvements in electrocatalysis[12,24]. Moreover, the *d*-density of states of Pt atoms was calculated to visualize the Pt *d*-band center (Fig. 4c & Supplementary Fig. 30). The Pt *d*-band center of strained PtPdFeCoNi HEA (221) (−2.30 eV) shifts downward after introducing compressive strain driven by surface stress release relative to those of defect-free PtPdFeCoNi HEA (111) (−2.19 eV) and Pt (111) (−2.13 eV). As the down-shift of the *d*-band center generally indicates increasing inertness of surface atoms, the surface Pt sites of PtPdFeCoNi HEA NRs with particular compressive strain interact less strongly with oxygenated adsorbates. This is indeed observed for $_{ad}$OH adsorption energy (a well-known descriptor of the ORR activity), which is significantly weakened on terrace sites of strained PtPdFeCoNi HEA (221) surfaces relative to PtPdFeCoNi HEA (111) (Fig. 4d). The distributions of *d*-band centers and surface $_{ad}$OH adsorption energies based on the local bonding environments of terrace Pt sites on strained PtPdFeCoNi HEA (221) can be inspected in Supplementary Fig. 31.

In addition, the performance of strained PtPdFeCoNi HEA (221) and PtPdFeCoNi HEA (111) are compared from the Gibbs free energy diagrams of the ORR pathway. At a potential of U = 0 V, the strained PtPdFeCoNi HEA (221) exhibits a more energetically favorable pathway than PtPdFeCoNi HEA (111) (Fig. 4e). It has been well established that OH desorption to produce OH^- is the potential-determining step due to the overly strong affinity of oxygenated species over the metallic Pt site[25]. This leads to sluggish ORR kinetics, a common problem of conventional Pt-based nanoparticles. At U = 1.23 V, strained PtPdFeCoNi HEA (221) exhibits a lower reaction barrier (0.88 eV) relative to that of PtPdFeCoNi HEA (111) (1.09 eV), indicating more facile OH desorption and accelerated ORR kinetics on particular compressive strain modulated PtPdFeCoNi HEA NRs, consistent with the experimental observations (Fig. 4f). Notably, the terrace Pd sites of strained PtPdFeCoNi HEA (221) also exhibit electronic structures and energetic reaction pathways similar to those of terrace Pt sites (Supplementary Fig. 32). Besides, the lower energy barrier for forming *OOH on strained PtPdFeCoNi HEA (221) implies the facile dissociation of the O–O bond and formation of *O intermediates in the subsequent steps. Therefore, the terrace Pt and Pd sites with particular compressive strain driven by stress release on PtPdFeCoNi HEA NRs can logically attenuate OH adsorption and promote ORR performance (Fig. 4g).

Discussion

In summary, we report a general method for synthesizing a class of HEA NRs equipped with abundant atomic terrace-type defects on interior and outside edges as high-performance ORR electrocatalysts. These terrace-type defects break the surface atomic symmetry to induce the release of intrinsic surface stress, generating the particular compressive strain. Experimental and theoretical investigations unveil that the intrinsic compressive strain can optimize the *d*-electron distributions of terrace Pt atoms, lowering the *d*-band center of Pt sites, thus leading to the facility of OH desorption, the acceleration of ORR kinetic and the minimization of ORR barrier. As a result, the representative PtPdFeCoNi HEA NRs deliver high mass and specific activities, with considerably elevated kinetics and good durability.

Methods

Materials

Palladium (II) acetylacetonate ($Pd(acac)_2$, 99%), iron (III) acetylacetonate ($Fe(acac)_3$, 98%), nickel (II) acetylacetonate ($Ni(acac)_2$, 95%), zinc (II) acetylacetonate ($Zn(acac)_2$, 97%), cobalt (III) acetylacetonate ($Co(acac)_3$, 98%), potassium hydroxide (KOH, 95%) and oleylamine ($C_{18}H_{35}NH_2$, OAm, 80%) were all purchased from Aladdin. Platinum (II) acetylacetonate ($Pt(acac)_2$, 97%) was obtained from Innochem. Manganese (II) acetylacetonate ($Mn(acac)_3$, 98%) and ammonium bromide (NH_4Br, 99%) were acquired from Adamas. Nafion (5 wt%) and tungsten carbonyl ($W(CO)_6$, 99%) were provided by Sigma-aldrich. Isopropanol (C_3H_8O, GR.), ethanol (C_2H_5OH, AR.) and cyclohexane (C_6H_{12}, AR.) were supplied by Sinopharm Chemical Reagent Co. Ltd. (Shanghai, China). Commercial carbon supported Pt catalyst (Pt/C, 20 wt% of 3 nm-Pt nanoparticles on carbon black) was provided by Johnson-Matthey Corp. All reagents were used without further purification, and all solutions were freshly prepared with ultrapure water (18.2 MΩ cm^{-1}).

Preparation of HEA NRs

In a typical preparation of quinary PtPdFeCoNi HEA NRs, $Pt(acac)_2$ (4 mg, 0.01 mmol), $Pd(acac)_2$ (5 mg, 0.016 mmol), $Fe(acac)_3$ (3.5 mg, 0.01 mmol), $Co(acac)_3$ (4 mg, 0.011 mmol), $Ni(acac)_2$ (3 mg, 0.012 mmol), NH_4Br (20 mg, 0.2 mmol) and $W(CO)_6$ (20 mg, 0.057 mmol) were dissolved in 5 mL of OAm by ultrasonicating for around 1 h. The mixture was then heated in an oil bath at 150 °C for 5 h under magnetic stirring. The precipitates were collected by centrifugation and washed two or three times with a cyclohexane/ethanol mixture. The preparation of septenary PtPdMnFeCoNiZn HEA NRs was similar to that of quinary PtPdFeCoNi HEA NRs except for adding $Zn(acac)_2$ (4 mg, 0.015 mmol) and $Mn(acac)_3$ (3 mg, 0.009 mmol) into reaction system.

Preparation of PtPdFeCoNi HEA NPs

The preparation for PtPdFeCoNi HEA NPs was similar to that of PtPdFeCoNi HEA NRs except for changing the feeding amount of NH_4Br to 15 mg (0.15 mmol) and the absence of $W(CO)_6$.

Characterizations

XRD experiment and data processing. Powder X-ray diffraction (XRD) experiments were performed using a Rigaku Smartlab SE X'Pert Powder diffractometer, equipped with a Cu-K_α X-ray source possessing a wavelength (λ) of 1.5406 Å. Calibration was carried out using a standard sample (Si) in accordance with the operating procedures to record the zero-point error of the instrument. 25 mg of dried powder sample was ground to 200–300 mesh and placed on the sample holder, compacted and flattened with a glass plate, keeping them at the same level as the edge of the groove. The operation voltage and current were 40 kV and 40 mA, respectively. The scanning range was set from 5 to 90 degrees, with a scanning speed step set at 0.02 degrees and an integration time of 0.6 seconds per step. The Rietveld refinement of XRD data is conducted using TOPAS software.

TEM experiment and data processing. Transmission electron microscopy (TEM) images were acquired on a JEM-1400 transmission electron microscope at an acceleration voltage of 100 kV. The products were dispersed in n-hexane, sonicated, and then drop cast onto a holey carbon support film of Cu 300 mesh grids for TEM testing. Aberration-corrected high-angle annular dark-field scanning transmission electron microscopy (HAADF-STEM) and corresponding elemental analysis were conducted on FEI Theims Z TEM instruments with an accelerating voltage of 300 kV. The precise atomic structures in HAADF-STEM images were analysed using Digital Micrograph software.

ICP-OES experiment and data processing. The composition of each catalyst was analysed by inductively coupled plasma optical emission spectroscopy (ICP-OES) (Thermo Fisher iCAP PRO). Operational parameters included RF Power at 1150 W, Plasma flow of 0.5 L min^{-1}, Auxiliary flow set at 0.5 L min^{-1}, Nebulizer flow at 12.5 L min^{-1}, and a sample uptake delay of 30 s. The catalysts were digested in aqua regia freshly mixed with 30% HCl (Kermel) and 65% HNO_3 (Kermel) in a volumetric ratio of 3:1, respectively. After digestion, the final concentration was in the range of 0–10 ppm by dilution with 2–5% dilute nitric acid. When analysing with ICP-OES, ultrapure water was first used as a blank sample to calibrate the instrument's baseline signal and ensure the accuracy of the measurement results. A series of multi-element standards (containing Pt, Pd, Fe, Co, and Ni) at different concentrations (0.1, 0.5, 1.0, 2.0, 4.0, 10.0 and 16.0 ppm) were then introduced into the instrument to measure the emission intensity for the elements in each standard. The calibration curves were generated by establishing the relationship between the standards' concentrations and the emission spectral intensities, which were further validated using samples of known concentrations. The contents of each element in the samples were calculated by measuring the intensities of the emission characteristic spectra and using the calibration curves.

XPS experiment and data processing. X-ray photoelectron spectroscopy (XPS) was acquired using a Thermo Scientific K-Alpha instrument, which is equipped with an Al-K_α (1486.6 eV) X-ray source. Before the XPS test, the powder samples (2 mg) were adhered to a sample holder using double-sided carbon conductive tape. The vacuum degree in the test chamber was less than 10^{-9} Pa, and the scan range was 1350– −10 eV. The steps of survey scan and high-resolution scan were 1 eV and 0.1 eV, respectively. The survey scan power was set to 12 kV × 6 mA with a pass energy of 150 eV, and the high-resolution scan power was set to 12 kV × 6 mA with a pass energy of 50 eV. Each sample was fixed at the same position for three consecutive tests to ensure the reliability of the data. Data analysis is conducted using XPSPEAK software, with all test results calibrated utilizing the C 1*s* peak at 284.8 eV.

AFM experiment and data processing. Prior to AFM imaging, the washed product was dispersed in 10 mL of cyclohexane via ultrasonication for 10 min to minimize aggregation. A 10 μL of dispersion was then drop-casted onto a freshly cleaved mica substrate and air-dried in a nitrogen environment. AFM was performed in tapping mode with Bruker Dimension ICON under ambient conditions with a scan rate of 1 Hz. The AFM probe (Bruker RTESPA-300, nominal spring constant 40 N/m) was calibrated using the thermal tune method prior to measurement. The image flattening and noise reduction were applied using the NanoScope Analysis software (v. 1.40) to enhance data interpretation.

XAFS experiment and data processing. X-ray absorption near-edge structure (XAFS) spectra of Pt L_3-edge were collected at the BL11B beamline of the Shanghai Synchrotron Radiation Facility (SSRF) using a fixed-exit double-crystal Si (311) monochromator at transmission mode for Pt foil and fluorescence mode for samples. The fluorescence

signals were collected with a Lytle detector, and the energy was calibrated with Pt foil. The calibration, pre-edge linear correction, and post-edge linear normalization of the collected XAFS raw data were systematically processed in the Athena module of the IFEFFIT software package based on the standard procedures. The Fourier transform fitting analysis of extended X-ray absorption fine structure (EXAFS) data was conducted on the Artemis program in IFEFFIT[26]. The parameters were configured as follows: k^2-weighting and k-space to R-space range of 3–12.4 $Å^{-1}$.

Electrocatalytic measurements. Before electrocatalytic measurements, as-synthesized PtPdFeCoNi HEA NRs and PtPdFeCoNi HEA NPs were deposited onto the commercial carbon supports (Ketjen Black-300) via continuous ultrasound. Specifically, PtPdFeCoNi HEA NRs and PtPdFeCoNi HEA NPs were dispersed in n-hexane, and the Ketjen carbon supports were dispersed in ethanol. Two as-obtained dispersed solvent were mixed under the ultrasonic environment for 3 h. The final products were collected via centrifugation, and then washed by acetic acid (36 wt%) for another 2 h to remove excess surfactants around the surface of catalysts. Finally, the collected products were washed with ethanol for several times to obtain the tested carbon-supported catalysts.

The electrochemical test catalyst ink was prepared as follows: 1 mg of the carbon-supported catalyst powder was dispersed into 1 mL of a solution containing 750 µL of water, 245 µL of isopropanol, and 5 µL of 5 wt% Nafion solution via sonication for 30 min at 25 °C. The yielded uniform ink was used to prepare the working electrode. Before catalyst coating, the glassy-carbon electrode (GCE, 5 mm, 0.196 cm^2) was polished with alumina polishing slurries, cleaned in an ultrasonic bath with ultrapure water, and dried naturally. Subsequently, 10 µL of ink was loaded onto a clean GCE, placed on a rotator, and spun at 300 rpm to remove solvent to form a smooth thin film. The concentration of platinum group metal (PGM) was determined by ICP-OES to be ~10.5 $µg_{PGM}\,cm^{-2}$. The saturated calomel electrode (SCE) and Pt foil were served as reference and counter electrodes, respectively. All the electrochemical measurements were conducted on a CHI 760E (Chenhua, Shanghai) electrochemical workstation with a typical three-electrode configuration. The 0.1 M KOH electrolyte for electrochemical measurements was freshly prepared by dissolving 2.82 g of KOH in 500 mL of deionized water and stored at 25 °C with dry ventilation. The electrolyte was remade daily. All the recorded potentials were calibrated to the reversible hydrogen electrode (RHE) according to the following equation: $E_{vs.\ RHE} = E_{vs.\ SCE} + 0.059\,pH + 0.241$. The actual pH value of 0.1 M KOH electrolyte was determined to be 13.18 ± 0.15. The reference electrode was calibrated against a RHE using hydrogen oxidation/evolution reaction (HOR/HER) polarization curves on a Pt/C working electrode. The Tafel slopes were obtained by transforming the ORR polarization curves with the Tafel formula and fitting the line segments in the kinetic region. The voltage range of the selected curve was near the starting potential to the half-wave potential.

Before ORR tests, the catalysts were activated by conducting the CVs to be stable in N_2-purged 0.1 M KOH at a sweep rate of 500 mV s^{-1}. The positive-going ORR polarization curves were tested in O_2-saturated 0.1 M KOH at a sweep rate of 20 mV s^{-1} and a rotation rate of 1600 rpm. All given ORR polarization curves were iR-corrected by 95%. Each electrochemical curves were carried out at least three times to obtain the corresponding standard deviations. The Tafel plots were analysed based on the kinetic-controlled region (around 0.85 and 0.95 V (vs. RHE) for commercial Pt/C and the HEA catalysts, respectively) of the ORR polarization curves (scan rate of 20 mV s^{-1}). The CVs were also recorded in N_2-purged 0.1 M KOH with a sweep rate of 50 mV s^{-1}. The accelerated durability tests (ADTs) were carried out in 0.1 M KOH by conducting the CVs between 0.6 and 1.0 V (*vs.* RHE) at a scan rate of 100 mV s^{-1} for different potential cycles.

The electrochemically active surface areas (ECSAs) of various catalysts were determined from charges associated with the stripping of CO. Specifically, the working electrode was placed into the 0.1 M $HClO_4$ electrolyte continuously purged with pure CO gas, and performed chronoamperometric tests at 0.1 V vs. RHE for 10 min. Then the working electrode was quickly moved into the other fresh N_2-purged 0.1 M $HClO_4$ and recorded two cyclic voltammograms (CVs) at a scan rate of 20 mV s^{-1}. The ECSA of the noble metals was calculated by the integral area of CO stripping and using Eqs. (1) and (2).

$$Q_{co-adsorption}(C) = \frac{\int idE(mAV)}{\nu(mV/s)} \tag{1}$$

$$ECSA\left(\frac{m^2}{g}\right) = \left[\frac{Q_{co-adsorption}(C)}{420\left(\mu\frac{C}{cm^2}\right)M_{PGM}(mg)}\right]10^5 \tag{2}$$

Calculation setup. Theoretical simulations were conducted using the Vienna Ab initio Simulation Package (VASP) based on density functional theory (DFT), employing the Projector-Augmented-Wave (PAW) pseudopotentials. For the treatment of electron exchange-correlation interactions, the Perdew-Burke-Ernzerhof (PBE) functional under the generalized gradient approximation (GGA) was adopted. The special quasi-random structure (SQS) representing the high-entropy alloy was generated via the Monte Carlo SQS (MCSQS) method as implemented in the Alloy Theory Automation Toolkit (ATAT)[27]. A face-centered cubic (fcc) supercell containing 32 atoms was used throughout the study. A plane-wave cutoff energy of 500 eV was applied in all computations. Structural relaxation was performed using a Gamma-centered 3×2×1 k-point grid. During geometry optimization, the top two atomic layers were allowed to relax until the force on each atom was below 0.02 eV $Å^{-1}$ and the energy convergence criterion was within 10^{-5} eV. The structures are supplied in Supplementary Data 1. Spin polarization was included in all calculations.

Data availability

The data generated in this study are provided in the Supplementary Information and Source Data file. Source data are provided with this paper.

References

1. Jiao, K. et al. Designing the next generation of proton-exchange membrane fuel cells. *Nature* **595**, 361–369 (2021).
2. Ellingsen, L. A. W. et al. Nanotechnology for environmentally sustainable electromobility. *Nat. Nanotechnol.* **11**, 1039–1051 (2016).
3. Shao, M. et al. Recent advances in electrocatalysts for oxygen reduction reaction. *Chem. Rev.* **116**, 3594–3657 (2016).
4. Capdevila-Cortada, M. A fine adjustment. *Nat. Catal.* **6**, 3 (2023).
5. Luo, M. & Koper, M. T. M. A kinetic descriptor for the electrolyte effect on the oxygen reduction kinetics on Pt(111). *Nat. Catal.* **5**, 615–623 (2022).
6. Tao, L. et al. Precise synthetic control of exclusive ligand effect boosts oxygen reduction catalysis. *Nat. Commun.* **14**, 6893 (2023).
7. Ma, Z. et al. Enhancing oxygen reduction activity of Pt-based electrocatalysts: from theoretical mechanisms to practical methods. *Angew. Chem. Int. Ed.* **132**, 18490–18504 (2020).
8. Chattot, R. et al. Beyond strain and ligand effects: microstrain-induced enhancement of the oxygen reduction reaction kinetics on various PtNi/C nanostructures. *ACS Catal.* **7**, 398–408 (2017).
9. Zhu, X. et al. Intrinsic ORR activity enhancement of Pt atomic sites by engineering the *d*-band center *via* local coordination tuning. *Angew. Chem. Int. Ed.* **60**, 21911–21917 (2021).
10. Escudero-Escribano, M. et al. Tuning the activity of Pt alloy electrocatalysts by means of the lanthanide contraction. *Science* **352**, 73–76 (2016).

11. Yang, C. et al. Sulfur-anchoring synthesis of platinum intermetallic nanoparticle catalysts for fuel cells. *Science* **374**, 459–464 (2021).
12. Tao, L. et al. A general synthetic method for high-entropy alloy subnanometer ribbons. *J. Am. Chem. Soc.* **144**, 10582–10590 (2022).
13. Wang, Y. et al. Ordered mesoporous high-entropy intermetallics for efficient oxygen reduction electrocatalysis. *Adv. Energy Mater.* **14**, 2303923 (2024).
14. Pedersen, J. K. et al. Bayesian optimization of high-entropy alloy compositions for electrocatalytic oxygen reduction. *Angew. Chem. Int. Ed.* **60**, 24144–24152 (2021).
15. Zhao, X. et al. Multiple metal-nitrogen bonds synergistically boosting the activity and durability of high-entropy alloy electrocatalysts. *J. Am. Chem. Soc.* **146**, 3010–3022 (2024).
16. He, T. et al. Mastering the surface strain of platinum catalysts for efficient electrocatalysis. *Nature* **598**, 76–81 (2021).
17. Strasser, P. et al. Lattice-strain control of the activity in dealloyed core-shell fuel cell catalysts. *Nat. Chem.* **2**, 454–460 (2010).
18. Wang, H. et al. Direct and continuous strain control of catalysts with tunable battery electrode materials. *Science* **354**, 1031–1036 (2016).
19. Liu, G. et al. Site-specific reactivity of stepped Pt surfaces driven by stress release. *Nature* **626**, 1005–1010 (2024).
20. Wang, L. et al. Tunable intrinsic strain in two-dimensional transition metal electrocatalysts. *Science* **363**, 870–874 (2019).
21. Sun, Y. et al. Ultrathin PtPd-based nanorings with abundant step atoms enhance oxygen catalysis. *Adv. Mater.* **30**, 1802136 (2018).
22. Luo, M. et al. PdMo bimetallene for oxygen reduction catalysis. *Nature* **574**, 81–85 (2019).
23. Chen, C. et al. Highly crystalline multimetallic nanoframes with three-dimensional electrocatalytic surfaces. *Science* **343**, 1339–1343 (2014).
24. He, L. et al. Single-atom Mo-tailored high-entropy-alloy ultrathin nanosheets with intrinsic tensile strain enhance electrocatalysis. *Nat. Commun.* **15**, 2290 (2024).
25. Gao, R. et al. Pt/Fe_2O_3 with Pt-Fe pair sites as a catalyst for oxygen reduction with ultralow Pt loading. *Nat. Energy* **6**, 614–623 (2021).
26. Ravel, B. & Newville, M. ATHENA, ARTEMIS, HEPHAESTUS: data analysis for X-ray absorption spectroscopy using IFEFFIT. *J. Synchrotron Radiat.* **12**, 537–541 (2005).
27. Van de Walle, A. et al. Efficient stochastic generation of special quasirandom structures. *Calphad* **42**, 13–18 (2013).

Acknowledgements

S.J.G., Y.S.Y. and M.G.L. acknowledged the support of the National Natural Science Foundation of China (Nos. 52271170 (Y.S.Y.), 52471198 (Y.S.Y.), 52303361 (M.G.L.), 52025133 (S.J.G.)), Heilongjiang Natural Science Funds for Distinguished Young Scholar (Grant No. JQ2023E004 (Y.S.Y.)), Beijing Outstanding Young Scientist Program (JWZQ20240102004 (S.J.G.)), the Fundamental Research Funds for the Central Universities (No. HIT.OCEF. 2021025 (Y.S.Y.)) and State Key Laboratory of Urban Water Resource and Environment (Harbin Institute of Technology) (No. 2022TS38 (Y.S.Y.)). The numerical calculations in this paper have been done on Hefei advanced computing center. The authors thank the photoemission BL11B in the Shanghai Synchrotron Radiation Facility (SSRF) for the help with XAFS characterizations.

Author contributions

L.H., M.G.L., and L.Y.Q. contributed equally to this work. S.J.G., W.W.Y., and Y.S.Y. conceived the project. L.H. designed the experiments. L.H., M.G.L, L.Y.Q., and M.C.L. performed data analysis and experiments discussions. L.Y.Q., F.Y.T., J.S. and X.Z. carried out the DFT simulations. X.R. conducted the schematic illustration. Y.Q.L. conducted HAADF-STEM and HRTEM measurements and data analyses. L.H., M.G.L., and L.Y.Q. wrote the paper. All authors discussed the results and commented on the manuscript.

Competing interests

The authors declare no competing interests.

Additional information

Supplementary information The online version contains supplementary material available at https://doi.org/10.1038/s41467-025-65856-z.

Correspondence and requests for materials should be addressed to Yongsheng Yu, Weiwei Yang or Shaojun Guo.

Peer review information *Nature Communications* thanks Qin Yue, and the other, anonymous, reviewer(s) for their contribution to the peer review of this work. A peer review file is available.